Available online at www.sciencedirect.com

ELSEVIER

Polymer 44 (2003) 4249–4260

polymer

www.elsevier.com/locate/polymer

Real time development of structure in partially molten state stretching of PP as detected by spectral birefringence technique

Yutaka Koike, Miko Cakmak*

Institute of Polymer Engineering, University of Akron, Akron, OH 44325-0301, USA

Received 21 February 2003; received in revised form 28 April 2003; accepted 30 April 2003

Abstract

Our main focus in this study is to investigate the deformation behavior of PP in temperature range where the PP is partially molten using a newly developed uniaxial stretching system. This system allows the real time study of the structural reorganization processes as reflected in birefringence coupled with true stress and true strain at temperature and deformation rates used in industrial film process. This instrument revealed that birefringence–stress relationship is linear beyond an initial yielding point until the onset of strain hardening beyond which negative deviation from this linearity is observed. At lower strains the films were found to continue to change significantly during holding stage leading to increase in birefringence. These changes observed in holding stage decreases with decrease of stretching speed and temperature and with increase of total strain. Increased strain rates result in destruction of crystallites that involves block rotations of these regions leading to observation of lower birefringence at faster rates. The latter process generates large amount of stretched amorphous chains that gradually convert to crystalline state during holding.

Keywords: Online-birefringence; Uniaxial stretch; Polypropylene

1. Introduction

The fundamental understanding between the processing parameters: temperature, rate, extent of stretching and development of structural characteristics: orientation, crystal size, shape evolution, etc. is paramount to ultimately control the properties that are being sought. It is difficult if not impossible to elucidate the transitional structural changes that occur during rapid deformation using traditional 'after the fact' experimental investigations with traditional structural tools. For this purpose, we have been developing integrated on-line measurement systems where mechanical as well as structural parameters specifically birefringence are measured during the fast transient processes that take place during deformation [1] and heat treatment [2–5]. The real time on-line spectral birefringence technique developed in our group has been successfully applied to heat setting of pre-stretched material and uniaxial stretching of PET.

In the film stretching of polypropylene, it is typically first cast into an unoriented highly crystalline state. This cast film is then reheated to temperatures where the film partially melts and deformation takes place at these 'mushy' temperature regions where the melt and crystal forms of the same material coexist. Although there have been many 'after the fact' studies on the stretched PP films, there is a lack of understanding of how these structures are altered during the deformation at this mushy temperature range using real time measurement techniques. This area of structural evolution during deformation has been neglected partly as a result of experimental difficulties in tracking time dependent complex sequence of structural events; orientation, melting, recrystallization and relaxation operating simultaneous or sequential manner. The research in polypropylene stretching in partially molten state stretching has focused mainly on the after the fact experimentation [6–10] that does not necessarily reveal the structural sequence that take place during deformation.

In order to clarify the structural behavior during deformation from this partially molten state we investigated the deformation behavior of isotactic polypropylene at a series of temperatures mainly 140–160 °C using our new instrument.

---

* Corresponding author. Tel.: +1-330-972-6865; fax: +1-330-258-2339. *E-mail address:* cakmak@uakron.edu (M. Cakmak).

0032-3861/03/$ - see front matter © 2003 Elsevier Science Ltd. All rights reserved.
doi:10.1016/S0032-3861(03)00386-0

2. Experimental section

2.1. Material

Basic properties of the material investigated are shown in Table 1. Isotacticity index reported in this table was obtained as weight fraction by xylene insoluble method based on ISO 9113:1986. A TA instruments Model DSC 2920 was used to determine the melting point (mp) at a heating rate of 10 °C/min. We also scanned the samples after having annealed in the oven for 10 min at chosen stretching temperatures (Fig. 1). Crystallinity (X_c) is obtained using Eq. (1). Note that we can find the mp above 160 °C and crystallinity above 140 °C increase remarkably by annealing before stretching at each stretching temperature. The start of melt is 119 °C, the onset of melt point of the cast film is 149 °C, melting peak is 161 °C and the end of melt is 172 °C, respectively.

$$\begin{aligned} X_c\ (\%) &= \text{Enthalpy of fusion}/\Delta H^0 \\ \Delta H^0 &= 209\ \text{J/g}\ [11] \end{aligned} \tag{1}$$

2.2. Sample preparation

PP sheets of about 0.3 mm thickness are obtained by extrusion-casting using a 1″ Prodex extruder (230 °C) equipped with an 8″ sheet casting die onto a casting roll maintained at 40 °C. The birefringence of cast sheets are measured by Model L305 with L 133 A Babinet compensator (Gaertner Scientific Co), and were found to be effectively isotropic as the birefringence values were around 4×10^{-4} at 565 nm. The cast films were cut into dumbbell shape with narrowest width of 30 mm at 30 mm gauge when target final strain is over 2.5, and narrowest width of 16 mm at 30 mm gauge when target final strain ratio is below 2.5. The stretching direction was chosen as the original extrusion direction of the cast films.

The mounted samples were inserted into the sample chamber and equilibrated at the chosen temperature for 10 min. After this time, the samples were stretched with 2, 20 and 300 mm/min until engineering strain reached to 5.5. After the completion of stretching, the samples were held in the clamps for 10 min at 300 mm/min, 12 min at 20 mm/min or 40 min at 2 mm/min as stretching rate. Except the sample with 0 min holding time was rapidly cooled by water spray, all other samples were cooled by air to room temperature and then removed from the clamps. The standard stretching temperatures (T_{stretch}) are chosen as Eq. (2).

$$T_{\text{stretch}} = T_{\text{onset temperature of melting}} + (T_{\text{end of melting}} - T_{\text{onset of melting}})/3. \tag{2}$$

that corresponds to 160 °C. This is also used in industry as typical deformation temperature in biaxially oriented polypropylene film stretching (BOPP) process.

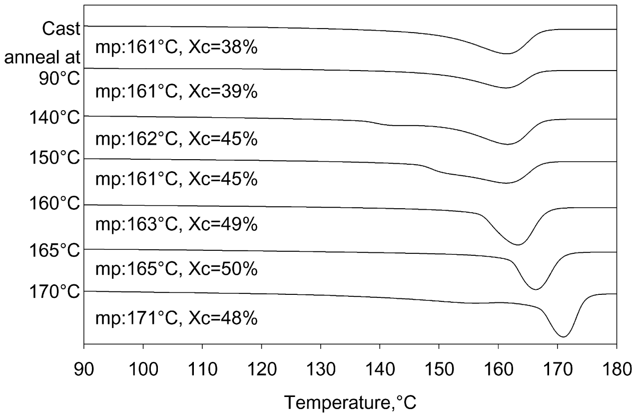

Fig. 1. DSC curves of cast sample and samples annealed for 10 min at indicated temperatures.

2.3. Instrumentation

The details of the stretching–birefringence apparatus were reported earlier [1]. Online-birefringence is essentially based on the method described by Posthuma de Boer et al. [12]. The characteristic of this method is using white light as light source to get the order number of retardation automatically. When we use the white light, representative light intensities through sample and a pair of cross polarizer is shown in Eqs. (3) and (4). Here I is light intensity. The term $e^{-2}\alpha$ accounts for attenuarion of light caused by scattering from the sample. Δn is birefringence and d is thickness of the sample.

$$I^{\perp} = \frac{I_0}{2} e^{-2\alpha} \sin^2\left(\frac{\pi \Delta n d}{\lambda}\right) \tag{3}$$

$$I^{\parallel} = \frac{I_0}{2} e^{-2\alpha} \cos^2\left(\frac{\pi \Delta n d}{\lambda}\right) \tag{4}$$

After detecting the light intensity of each component, the computer calculates normalization value of light intensity to

Table 1
Basic properties of the material

Material maker	Grade	MFR (g/10 min, 230 °C)	Isotacticity index (%)	DSC (ramp = 10 °C/min)		
				mp (°C)	T_c (°C)	Crystallinity (%)
Union Carbide	5D98 (for sheet)	3.4	95	161	106	38

erase the attenuation factor Eq. (5):

$$N^{\perp} = \frac{I^{\perp}}{I^{\perp} + I^{\parallel}} = \sin^2\left(\frac{\pi \Delta n d}{\lambda}\right) \tag{5}$$

The difference in period varied with the retardation. When we put t_{pi} to each peak of $\sin^2(\omega t)$, the period expresses as Eq. (6) follows.

$$\pi/\omega \equiv |t_{\mathrm{pi}+2} - t_{\mathrm{pi}}| \approx |2(t_{\mathrm{pi}+1} - t_{\mathrm{pi}})| \tag{6}$$

As t in $\sin^2(\omega t)$ corresponds to $1/\lambda$ in $\sin^2(\pi \Delta nd/\lambda)$ and ω in $\sin^2(\omega t)$ corresponds to $\pi\Delta nd$ in $\sin^2(\pi\Delta nd/\lambda)$, respectively, we get the following Eq. (7) which is relation between retardation and wavelength in peak of the normalized light intensity. Here R is retardation of sample.

$$R = \Delta nd \approx \lambda_{\mathrm{pi}+1}\lambda_{\mathrm{pi}}/(2|\lambda_{\mathrm{pi}+1} - \lambda_{\mathrm{pi}}|) \tag{7}$$

In our case we have automated this technique to obtain real time retardation measurements at about 3–5 Hz at 633 nm wavelength. Representative dispersion curves are also automatically determined by the following Eq. (8) in the range of 460–650 nm [13]. Here R_0 (nm) is the retardation at the infinite wavelength which is dependent on the degree of molecular orientation, and a is a material constant.

$$R \approx R_0 + a/\lambda^2 \tag{8}$$

In order to determine the birefringence, the thickness needs to be measured at the same time and at the same location where the birefringence is measured. This is accomplished using a laser micrometer that measures the width of the sample continuously. We then use the transverse isotropy assumption (Eq. (9)), $\epsilon_{\mathrm{TD}} = \epsilon_{\mathrm{ND}}$ to calculate real time thickness with the knowledge of the initial thickness. In order to validate this assumption, we performed a series of experiments where the samples were stretched to mainly 5.5X engineering stretch ratio and examined the thickness determined by the assumption given above and independently by cooling the sample down and determining the results by precision micrometer. As shown in Table 2, the difference between the two was found to be on the average within 4% of the actual value in these conditions. This difference becomes smaller above the onset of melt temperature. Thus the constrained strain caused by the chosen sample shape or severe necking is found to be avoided under these conditions given mushy state. Optical retardation is measured at the midsection of the sample with a light beam illuminating 8 mm diameter portion of the sample.

Generally speaking polymer in molten state shows incompressibility [14] and we also use the incompressibility assumption (Eq. (10)) to get the true strain under these partially molten state.

$$\text{Transverse isotropy}: W_{\mathrm{t}}/W_{\mathrm{o}} = D_{\mathrm{t}}/D_{\mathrm{o}} \tag{9}$$

$$\text{Incompressibility}: D_{\mathrm{o}}W_{\mathrm{o}}L_{\mathrm{o}} = D_{\mathrm{t}}W_{\mathrm{o}}L_{\mathrm{o}} \tag{10}$$

Using Eq. (9)

$$\text{Thickness} = D_{\mathrm{t}} = (W_{\mathrm{t}}/W_{\mathrm{o}})D_{\mathrm{o}} \tag{11}$$

Using Eqs. (9) and (10)

$$\text{True strain} = L_{\mathrm{t}}/L_{\mathrm{o}-1} = (W_{\mathrm{o}}/W_{\mathrm{t}})^2 - 1 \tag{12}$$

Using Eq. (9)

$$\text{True stress} = F_{\mathrm{t}}/(W_{\mathrm{t}}D_{\mathrm{t}}) = F_{\mathrm{t}}/\{(W_{\mathrm{t}}^2/W_{\mathrm{o}})D_{\mathrm{o}}\} \tag{13}$$

2.4. X ray measurements

Bruker AXS Generator equipped with a copper target tube and two-dimensional detector was used to obtain the unique one quadrant of the uniaxially oriented samples. The generator was operated at 40 kV and 40 mA and was beam was monochromatized at Cu Kα. Accumulation time of 30 min was used.

2.5. Herman's orientation factor

Herman's orientation factors (f) were calculated using infrared dichroism and WAXD [15] techniques. Phase specific bands previously identified by Samuel for PP was used for dichroism studies [16]. The chosen wavenumbers are as follows; crystal: 1045 cm^{-1}, transition moment angle (α_λ) = 0°, amorphous: 2720 cm^{-1}, $\alpha_\lambda = 90°$. The IR experiments were performed with 100 scans at 0.5 cm^{-1} wave number resolution. The baseline was determined horizontally as shown as H baseline in Ref. [17]. The samples were measured after one month room temperature conditioning. Their retardations were also measured by using Berek compensator.

Herman's orientation factor f is derived from Eqs. (14) using infrared dichroism.

$$f = \frac{D-1}{D+2} \times \frac{D_0+2}{D_0-1} \tag{14}$$

Here, D = absorbance in $\parallel$/absorbance in $\perp$, $D_0 = 2 \times \cos^2\alpha_\lambda/\sin^2\alpha_\lambda$

$$\alpha_\lambda = 0° \rightarrow D_0 = \infty, \quad \alpha_\lambda = 90° \rightarrow D_0 = \infty$$

This f value is also obtained by WAXS by using following Eqs. (15)–(17).

$$f_{c,z} = ((3\cos^2\chi_{c,z}) - 1)/2 \tag{15}$$

The main crystal system in polypropylene is α type which is monoclinic and the molecular chains are parallel to c axis, thus the square of the angle between c axis and the reference

Table 2
Shape in transformation

Temperature (°C)	Speed (mm/min)	Engineering strain	Difference $(1-((T/T_0)/(W/W_0)))$, (%)	T/T_0, (%)	W/W_0, (%)
170	300	5.5	−3.1	43	42
165	300	5.5	−2.3	42	41
160	300	0.35	−1.7	89	87
	300	1.3	−3.3	65	63
	300	3	3.1	48	50
	300	5.5	−2.8	42	41
	300	7.3	−4.0	39	38
	20	5.5	−4.7	42	40
	2	5.5	−5.2	40	38
150	300	5.5	−4.0	43	41
140	300	5.5	10.1	39	43
	20	5.5	−3.0	43	42
	2	5.5	−6.0	43	40
90	300	5.5	7.8	41	44
	2	5.5	4.7	42	44
Average of absolute value			4.4		

direction Z, $\cos^2\chi_{c,z}$ is described as follows when we take the (110) and (040) planes in this case.

$$\cos^2\chi_{c,z} = 1 - 1.099\cos^2\chi_{110,z} - 0.901\cos^2\chi_{040,z} \qquad (16)$$

Here, $\cos^2\chi_{hkl,c}$ is obtained from the following equation

$$\cos^2\chi_{hkl,z} = \frac{\sum_{0°}^{90°} I_{hkl}(\chi)\sin\chi\cos^2\chi}{\sum_{0°}^{90°} I_{hkl}(\chi)\sin\chi_z} \qquad (17)$$

3. Results and discussion

3.1. Deformation behavior

One of the key mechanical performance characteristics that govern the behavior of films during deformation is the yielding phenomenon. Particularly the stress drop after yielding in engineering stress strain curves is an indicative of the sharpness of the necks typically observed. This behavior is primarily controlled by the process variables such as rate of stretching and temperature. Fig. 2 shows that decrease of stretching rate and increase of temperature decreases this tendency to form sharp necks as also observed by others [7]. Increasing the stretching temperatures to 140 °C and beyond expands this stretching rate range where the apparent yielding is suppressed as more material gets melted and the overall structures unravel without significant localization of deformation.

Fig. 3 shows true stress–true strain curves. As we reported earlier [18], although stress overshoot can be seen in engineering stress–strain curves, the true stress shows a smooth transition change during stretching which reflects the intrinsic behavior of the material being investigated. Increasing temperature naturally reduces the stresses at all strain ranges including yield point. The onset of strain hardening appears around 5 MPa in these partially molten conditions. At the end of the stretching, the stress relaxation for specific time was monitored. In this stage, the stress relaxation decreases with the decrease of stretching speed. This indicates that at lower speeds the relaxation rate is comparable to stretching rates during deformation, and this greatly suppresses final relaxation levels. Another possibility is at high speeds, deformation generates sufficiently looser structure with greater fraction of original structure destroyed, resulting in larger relaxation to occur due to ‘loose’ structure. After holding for this time, the final true stress of the sample stretched at 300 mm/min stretching rate becomes smaller than those stretched at slower speed. In samples stretched to the same engineering strain, the true strain decreases with increasing speed (140 and 160 °C at Fig. 3). This comes from the difference in the effectiveness of stretching, at especially amorphous regions. That is, the samples in higher stretching rate are not stretched effectively, so the final stress and strain becomes smaller. The stress relaxation after stretching seems to occur mainly due to recovery of stretched amorphous regions.

The effect of stretching speed on the birefringence vs. true strain curves are shown in Fig. 4. The films stretched with highest stretching speed exhibit lower birefringence for a given true strain values. In addition, the sample that was stretched at the fastest speed shows the largest changes during the holding stage. These results suggests that at high rate of stretching, a significant destruction of crystalline regions occurs generating highly oriented amorphous chains that slowly convert to back to crystalline state while sample is maintained in constrained state by the grips.

Fig. 5 shows that birefringence does not begin to increase

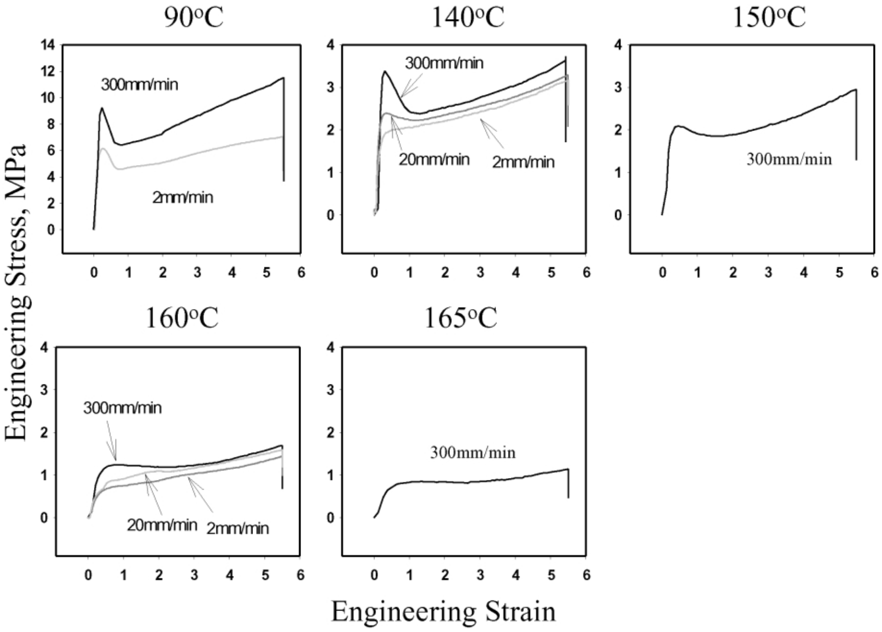

Fig. 2. Engineering Stress Strain curves.

substantially unless a critical stress level in each condition is passed. This position roughly corresponds to the start of the large plastic deformation. This occurs around yield point at engineering S–S curve as shown in Fig. 6 in which the arrows indicate the onset of increasing birefringence. Increasing temperature or decreasing speed shifts this starting point to lower stress levels. It is also interesting to note that the once the large birefringence changes start, it increases almost linearly with stress essentially following stress-optical law behavior until the onset of strain hardening at temperatures where the samples are partially molten.

Fig. 7 shows the effect of stretch ratio at 160 °C using 300 mm/min stretching rate. The true stress birefringence curves show that during plastic deformation there exist a linear relationship between the birefringence and true stress shown broken line in Fig. 7 suggesting that this stress-optical law with minor modifications can be extended to the partially molten state. In addition beyond about a critical stress of roughly 5 MPa, this response become non-linear in this mushy temperature. Below this critical stress levels the birefringence values were found to increase during holding stage suggesting that additional oriented crystallization may be taking place most possibly converting from the oriented

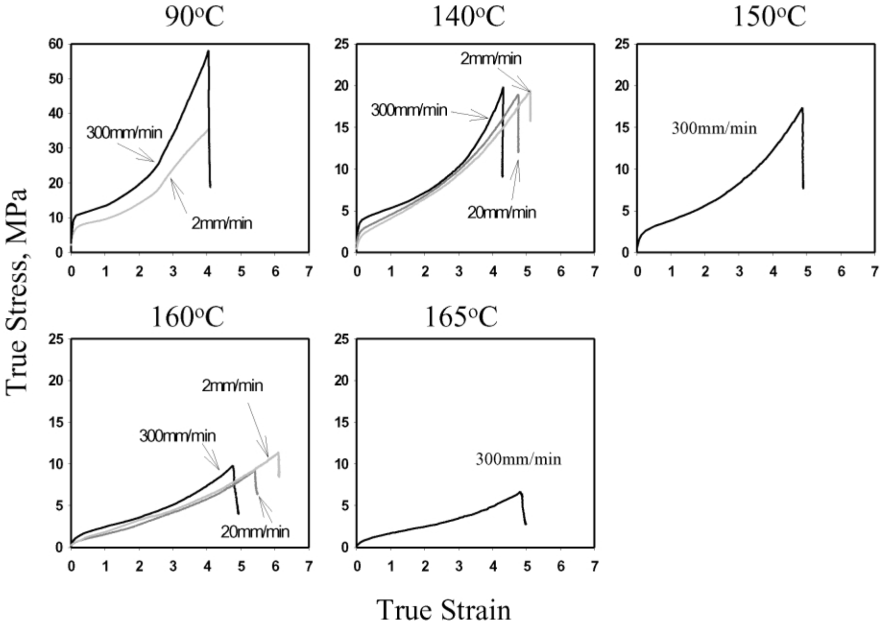

Fig. 3. True Stress Strain curves.

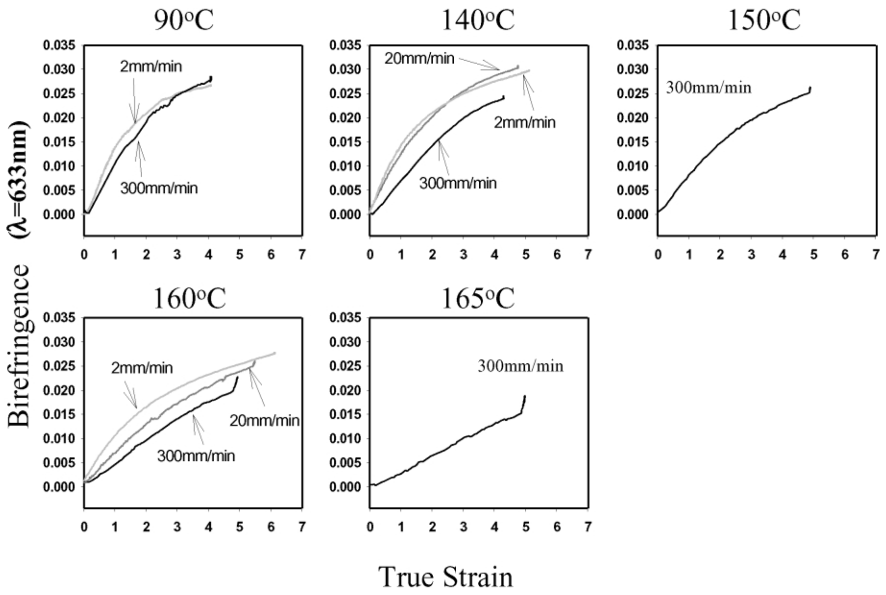

Fig. 4. Birefringence vs. True Strain.

amorphous regions. At higher stretch ratios than the onset of the strain hardening the slope of this holding stage decreases indicating the structure that has formed is mostly ‘locked in’ by the deformation suppressing further changes in the holding stage event at these fairly high temperatures. We observed similar behavior in stretched natural rubber earlier [1]. Fig. 8 shows the same effect at small strains. We can find there is little change in birefringence before stretching and even after stretching as long as the strain is in elastic transformation zone. We can see no significant change in birefringence just by heating the unstretched sample in the clamps.

3.1.1. Evaluation of stretched samples by off-line methods

Fig. 9 shows Herman’s orientation function of samples stretched at 160 °C, 300 mm/min. The orientation factor (f) in crystalline region (f_c) and amorphous region (f_{am}) increase in almost parallel with true strain till true strain 3 and there is not significant increase in the true strain greater than 3. The orientation data obtained from IR (1045 cm^{-1}) and X-ray match well, though f_c by XRD is greater than f_c (1045 cm^{-1}) in lower stretch ratio below 1.5.

We obtain the intrinsic values by usage of two phases model shown in the equation

$$\Delta n = X_c \Delta n_c^0 f_c + (1 - X_c)\Delta n_a^0 f_{am} + \Delta n_{form} \qquad (18)$$

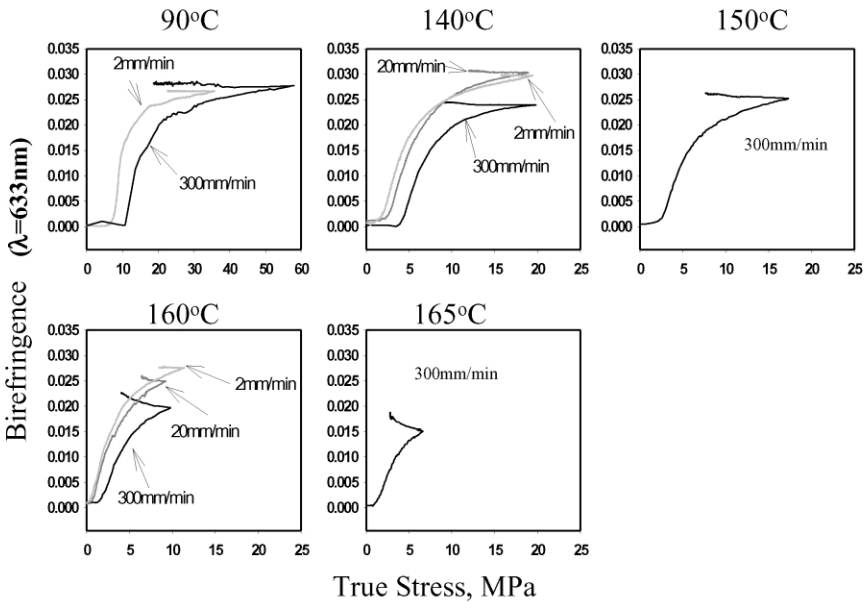

Fig. 5. Birefringence vs. True Strain.

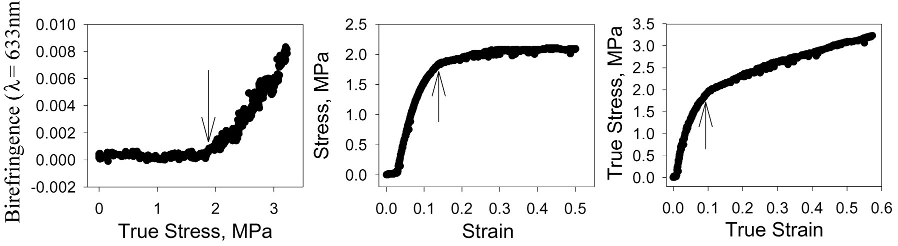

a) 140°C, 2mm/min.

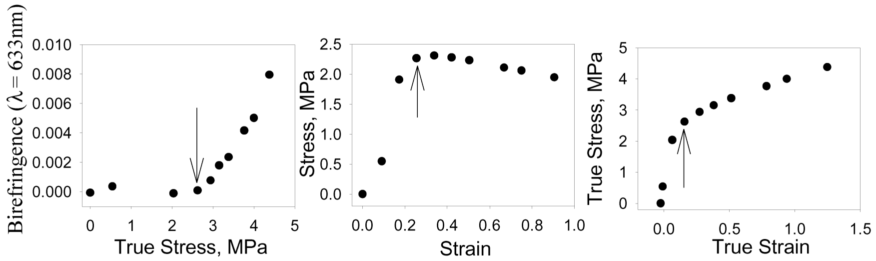

b) 150°C, 300mm/min.

Fig. 6. Initial part of stretching.

X_c is the crystallinity of the samples obtained by DSC. Conversion from weight fraction to volume fraction in X_c by using density of crystal and amorphous is 0.937 and 0.852 g/ml, respectively [11]. Each of Δn_c^0 and Δn_{am}^0 is intrinsic birefringence of crystalline region and amorphous region, respectively. Δn_{form} is called form birefringence that arises when there is an ordered arrangement of optically isotropic particles whose size is smaller than the wavelength of light and is ignored here.

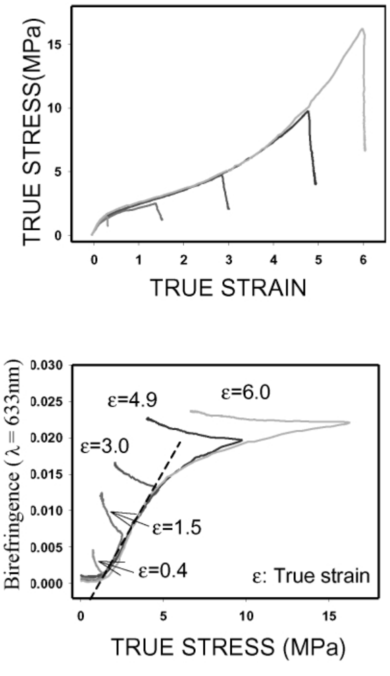

Fig. 7. Stretch ratio dependence at 160 °C, 300 mm/min.

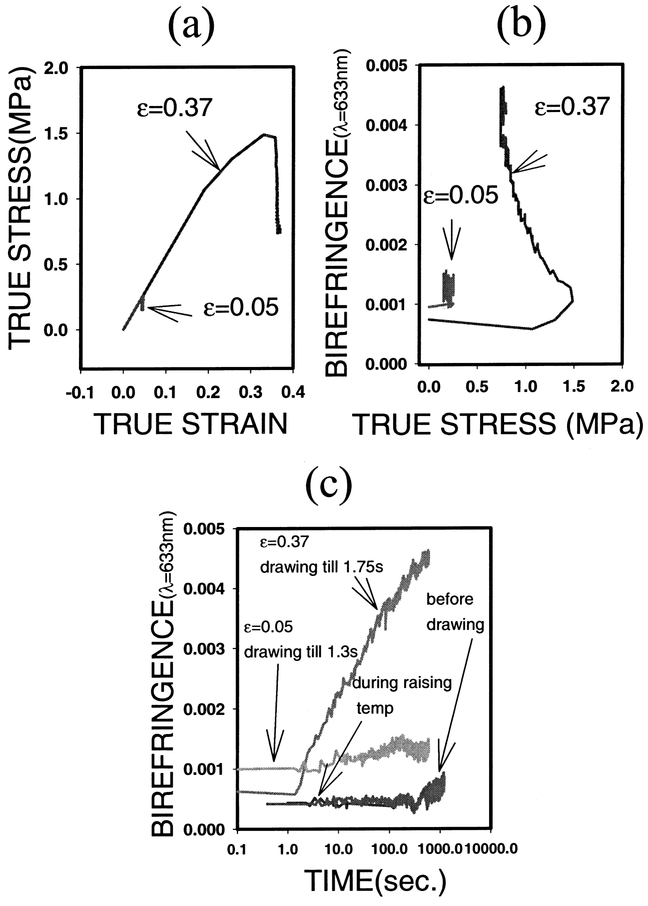

Fig. 8. Small strains at 160 °C, 300 mm/min.

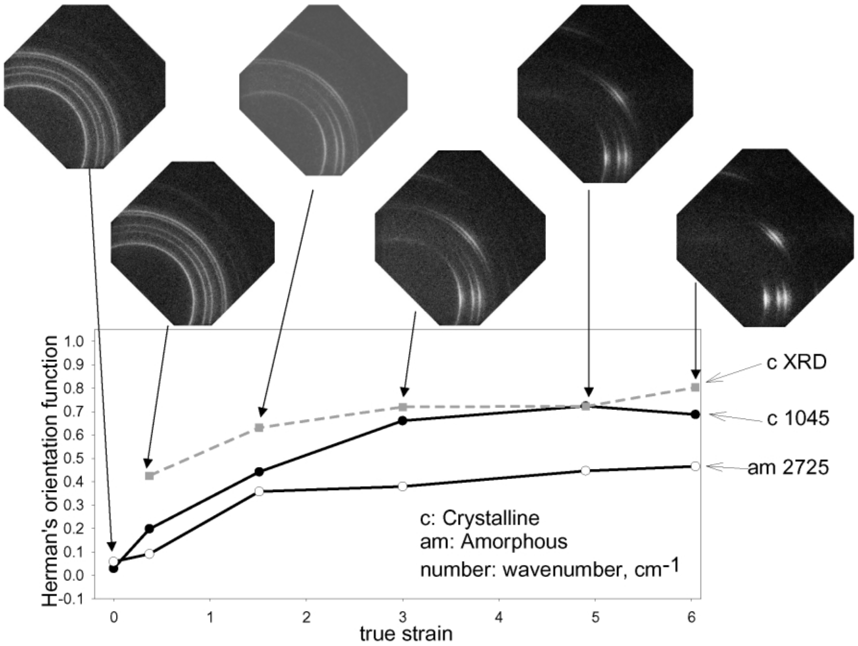

Fig. 9. Herman's orientation factor at 160° C, 300 mm/min.

Rearranging Eq. (18),

$$\Delta n/(X_c f_c) = \Delta n_c^0 + \Delta n_a^0 (1 - X_c) f_{am}/(f_c X_c) \tag{19}$$

The $\Delta n_c^0 = 0.0272$ is obtained from the intercept and $\Delta n_{am}^0 = 0.0670$ ($R^2 = 0.78$) from the slope of the plot of $\Delta n/(X_c f_c)$ against $(1 - X_c) f_{am}/(f_c X_c)$. These values agree with those reported by Samuels: $\Delta n_c^0 = 0.0285$ and $\Delta n_{am}^0 = 0.0618$ [19], $\Delta n_c^0 = 0.0291$ and $\Delta n_{am}^0 = 0.0600$ [20].

3.2. Behavior during holding

Next we look into what happens during the holding after stretch through on-line and off-line experiments. We take the samples stretched to around 1.3 true strain then hold them for various times ranging from 0 to 10 min after

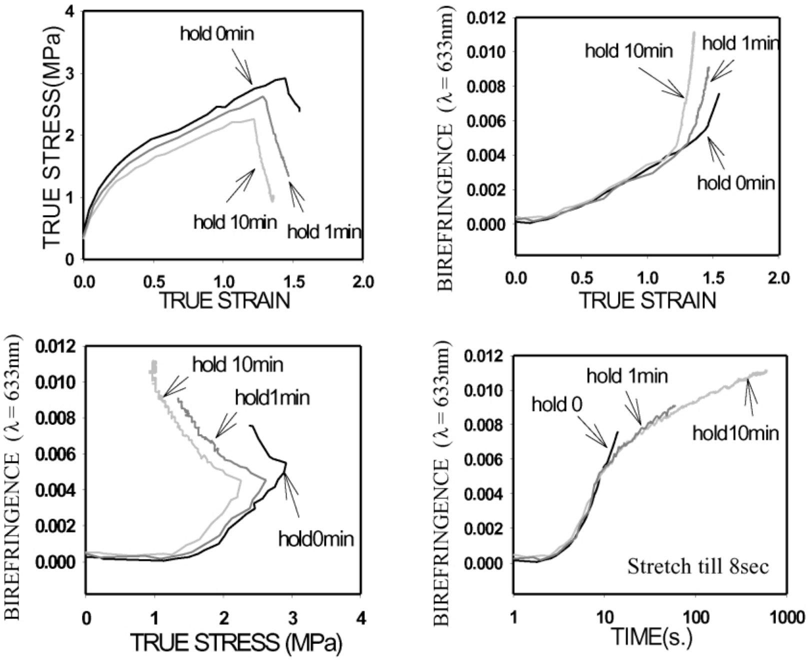

Fig. 10. Effect of holding time after stretching 300 mm/min, 160° C.

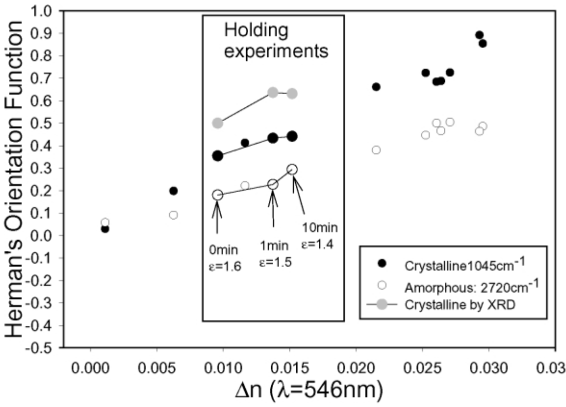

Fig. 11. Herman's orientation function including the holding time effects.

stretched at 300 mm/min, 160 °C. The sample with 0 min holding time was cooled by spraying water just after stretching is completed. We made these true strains similar but slightly higher in shorter holding time samples to eliminate the effect of strain itself. The on-line data of these samples are shown in Fig. 10. Thus even slightly smaller true strain results in higher birefringence after 10 min. Fig. 11 and 12 reveals that both of crystalline and amorphous orientation increase in parallel during the holding. Fig. 12 shows the crystal size obtained by Scherrer equation Eq. (20) obtained from WAXD data. In parallel with the above observation in orientation, the crystal sizes obtained from the equatorial planes also show an increase in crystallite size indicating the scale of crystallite thickening at this stage.

$$L(\text{Å}) = K\lambda/(\beta_{1/2}\cos(\theta)) \qquad (20)$$

Here, L, crystal size; $K = 1$; λ, wavelength of $K_\alpha = 1.542$ Å; $\beta_{1/2}$, halfwidth; θ, peak position.

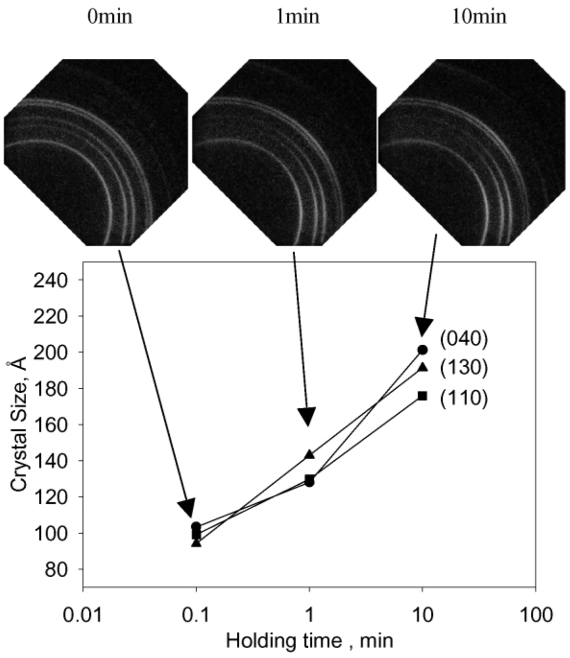

Fig. 12. Crystallite size change during holding.

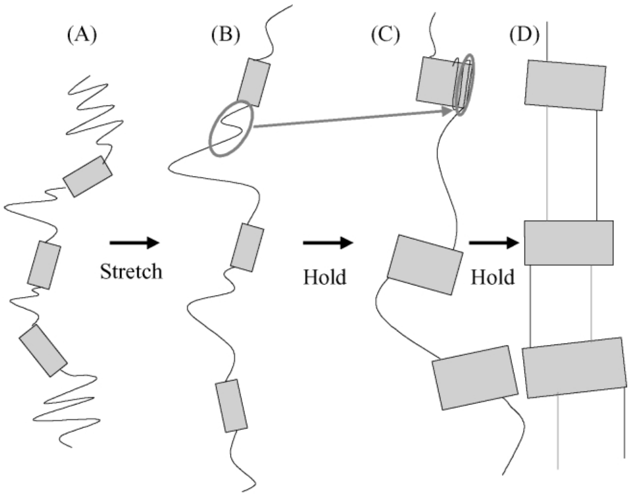

Fig. 13. Schematic of the molecular chain and crystallite rearrangement by crystallite thickening during holding.

We can see the crystallite thickening occurs while birefringence increases in Fig. 12.

3.3. Structural model

3.3.1. Mechanism of increasing orientation factor during holding

Structural characteristics of the deformation and holding are given in model shown in Fig. 13. Here we simplify the structure to depict this phenomenon plainly and just one microfibril which is combination of a series of the crystallite and tie molecular along the stretching direction and just one or two tie molecular chains are sketched. After the process of stretching, that is, the transformation of crystallite and amorphous chains finish, the adjacent parts of the molecular chains in the amorphous chains are used to thicken the crystallite (step C in Fig. 13) [21]. Thus the length of molecules in the amorphous regions become shorter and taut gradually (step C and step D in Fig. 13). At the same time, the taut tie molecular chains also tug at crystallites. As the crystallites have been aligned to stretch direction to some extent, the tug direction among crystallites through the tie molecular chains is also stretch direction. Thus not only f_{am} but also f_c increases in the parallel during the holding.

3.3.2. The difference in molecular rearrangement ability in each condition

As shown in Fig. 14, although the crystallites in the spherulite grow during the holding in unoriented films [22], because the direction of crystallite is random, the birefringence does not increase by their growth as shown in Fig. 8(c) (step A in Fig. 14). Once the material is stretched to some extent (step B in Fig. 14), there is substantial amount of molten material that is highly deformable. As the film is stretched, these regions undergo substantial orientation and orientation induced crystallization occurs. This process

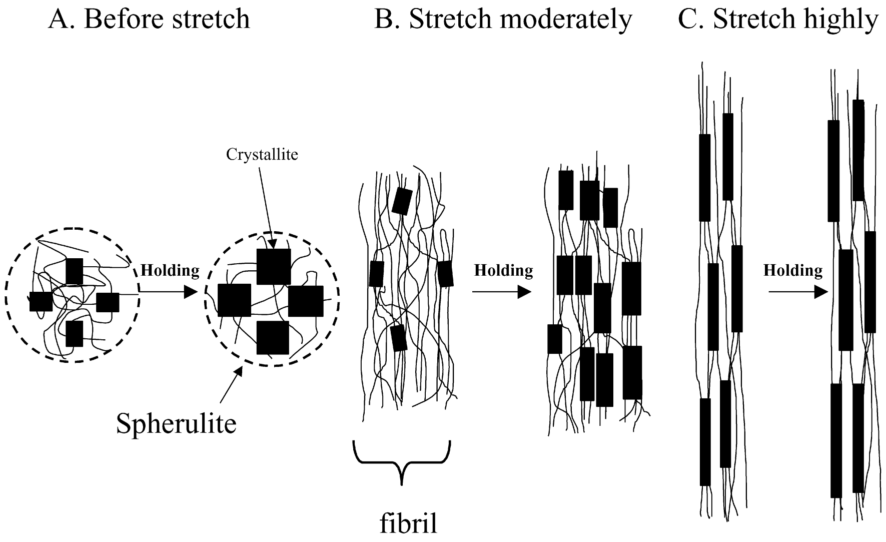

Fig. 14. Schematic of the stretching induced crystallization.

essentially is coupled with the partial break up and reorientation and recrystallization of the some of the preexisting crystallites. The latter two processes contribute to the increase of birefringence. However, at elevated temperatures, there remains a significant amount of molten/amorphous oriented chains that upon stoppage of deformation continue to rearrange and crystallize as the built up stresses are relieved leading to higher birefringence levels. This increase of birefringence is larger at lower strains and it decreases as the deformation levels increases. This indicates that the 'pool' of materials available to change decreases with increased deformation (step C in Fig. 14). The rate effect is also quite pronounced on the latter morphological picture. As the rate is increased, the crystallites are increasingly destroyed at the same strains leading to lower birefringences during stretching and since this process generates larger fraction of molten/amorphous fraction the holding stage involves significant levels of birefringence increase converting oriented amorphous chains to oriented crystalline regions or trapping these regions in amorphous but taut state as the crystallization proceeds.

3.3.3. Molecular orientation behavior in each stage

Fig. 15 is a schematic of the birefringence behavior. We divide the behavior into three sections. Zone I is from the initial of transformation to yielding point. Zone II is from

Table 3
Physical properties in the zone II

Temperature (°C)	Rate (mm/min)	Slope (Δn against σ, MPa^{-1})	True strain		True stress, (MPa)		Birefringence	
			Start	End	Start	End	Start	End
90	2	0.0069	0.32	1.04	7.98	9.67	0.0036	0.0142
140	2	0.0060	0.17	1.00	2.11	4.07	0.0032	0.0142
160	2	0.0059	0.02	1.22	0.32	2.13	0.0015	0.0121
90	300	0.0038	0.16	1.06	10.71	13.63	0.0002	0.0113
140	300	0.0042	0.16	1.67	3.92	6.44	0.0005	0.0119
160	300	0.0044	0.29	2.75	1.68	4.75	0.0010	0.0134
165	300	0.0031	0.19	3.04	0.77	3.57	0.0003	0.0103
Molten PP		0.00083	Stress optical coefficient of molten PP					

Table 4
Physical properties in the linear region in the latter part of the zone III

Temperature (°C)	Rate (mm/min)	Slope (Δn against σ, MPa^{-1})	True strain Start	True stress (MPa) Start	Birefringence Start
90	2	0.00015	2.8	30.2	0.024
140	2	0.00024	4.3	19.1	0.024
90	300	0.00017	2.5	17.2	0.024
140	300	0.00038	3.6	11.8	0.027

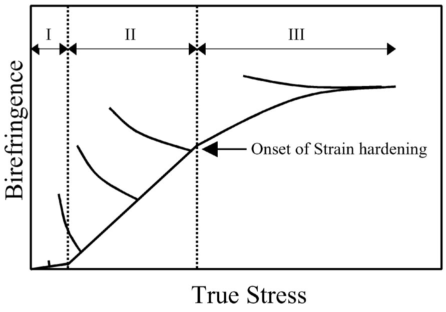

Fig. 15. Identified stages in the Birefringence vs. stress change during stretching and holding.

yielding point to onset of strain hardening. Zone III is after onset of strain hardening. Zone I is elastic zone. Birefringence increases slightly during the stretching and holding after stretching. The yield point in Zone II is the onset of the increase of birefringence. In this II zone, birefringence increases almost linearly. Physical properties and the slopes of birefringence against true stress in linear regions in Zone II and Zone III are shown in Tables 3 and 4, respectively. The slopes 165 °C and the below are greater than stress-optical coefficient [23] of the molten PP. The values of these physical properties vary with the temperatures and stretch rates. The end points of linear zone at slower speed occurs at lower strains. This means the slower the speed, the more effective the orientation, so the structural tightening process starts at lower strains. In zone III the birefringence increase is slower and starts deviating from the linear behavior observed in zone II and both of f_c and f_{am} also hardly increase as shown in Fig. 9. Some samples in lower temperature show linearity in the latter part in the Zone III. These slopes are smaller than stress-optical coefficient. In this region, the easily deformable body's has already been exhausted and the birefringence increase become increasingly difficult as the structure begins to 'lock in' as some of the chains become fully taut. The increase in birefringence in the holding stage is minimal.

4. Conclusions

A fully automated tensile stretcher/spectral birefringence system developed in our group was used to follow real time stress–birefringence–strain behavior during uniaxial stretching of polypropylene at 'mushy' temperature ranges. This allowed us to investigate the deformation behavior and resulting structural changes during stretching without having to stop and separately examine the sample being stretched and subsequently held in clamps undergoing relaxation.

This instrument revealed that birefringence–stress relationship is linear beyond an initial yielding point until a critical stress reached. This critical stress coincides with the onset of strain hardening in the partially molten state. At low strains the films were found to continue to change significantly during holding stage leading to increased crystallinity and orientation that increase the overall birefringence. This change in holding stage decreases with the increase in deformation that increasingly create oriented 'constrained' morphology. Increased strain rates result in destruction of crystallites that may also involve block rotations of these regions. The latter process generates large amount of stretched amorphous chains that gradually convert to crystalline state during holding.

Acknowledgements

We would like to thank the support of Asahi Kasei Corporation towards this research.

Appendix A

Each of crosshead separation rates (Eq. (21)) and Hencky true strain rates at the center of the sample (Eq. (23)) detected from the width measurements of the sample under incompressibility assumption (Poisson's ratio = 0.5) in several stretch conditions are shown in Fig. 16 (Strain rate of these experiments.).

Cross head separation rates

$$: \text{cross head separation speed (mm/s)}/\{L_o(1+\epsilon)\} \quad (21)$$

Hencky strain:

$$\epsilon^{H} = \int_{l_0}^{l} \frac{dl}{l} = \ln(1+\epsilon) \quad (22)$$

Here, ϵ is strain.

$$\text{Hencky true strain rate} = d\epsilon^{H}_{\text{true}}/dt \quad (23)$$

This Hencky true strain rate can be obtained from the time variation of width under transverse isotropy assumption Eq. (9).

$$\text{Width decreasing rate at each time} = d(\Delta W_t/W_t)/dt \quad (24)$$

Hencky true strain rate

$$= d(\Delta W_t/W_t)/dt/(\text{Poisson's ratio}) \quad (25)$$

The calculated crosshead separation speed, that is shown by line in Fig. 16, is maximum at the start and gradually decreases with deformation under constant crosshead separation speed. Hencky true strain rate of the sample, which is shown in the plots and R^2 value is calculated using the crosshead separation rates, starts at lower value than the crosshead separation rate. This is caused by the delay of response of the sample due to the initial slack, etc. When the sample begins to transform homogeneously, the Hencky

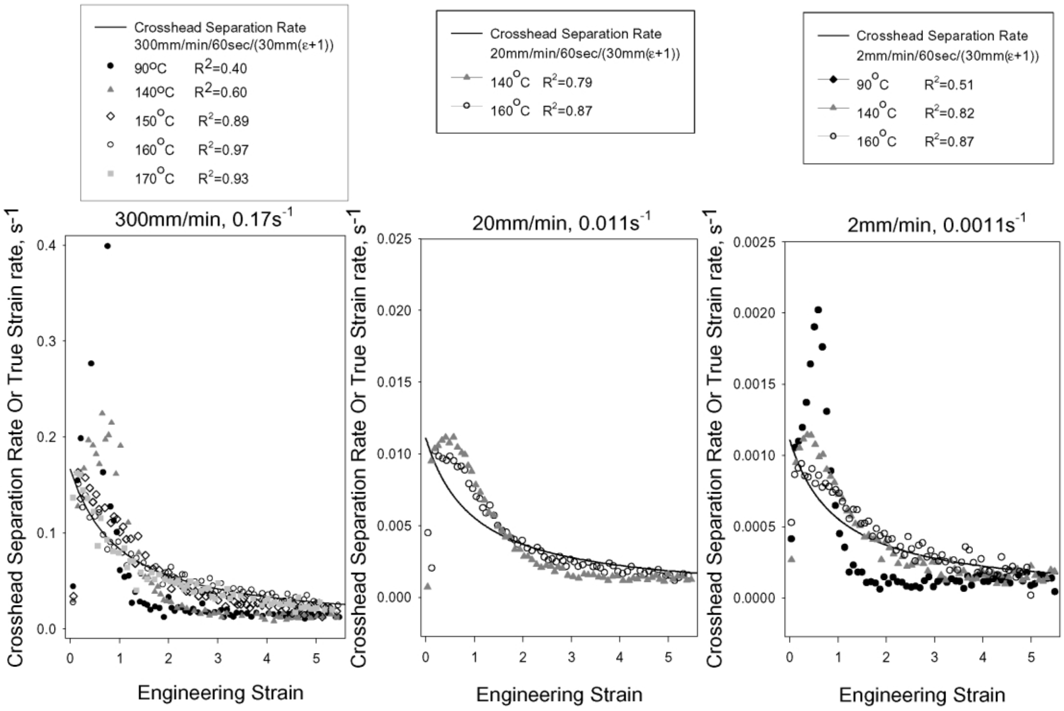

Fig. 16. Change of strain rate with strain.

true strain rate at the center of sample is the same as the crosshead separation speed. On the other hand, when sample shows necking, the initial part of Hencky strain rate is higher than crosshead separation speed due to localization of deformation. After that the Hencky strain rate becomes less than crosshead separation speed due to propagation of necking. We can see the large deviation in the crosshead separation rate at temperatures lower than 140 °C, especially 90 °C at which temperature the sample has not began to melt. This deviation at lower temperature becomes smaller at lower speeds where the necking is generally less pronounced. The deviation becomes smaller above 150 °C.

References

[1] Valladares D, Toki S, Sen TZ, Yalcin B, Cakmak M. Macromol Symp 2002;185:149–66.
[2] Cakmak M, Serhatkulu T, Kokturk G. In: Cunha AM, Fakirov S, editors. Structure development during polymer processing. NATO Science Series Series E, Applied Science, vol. 370. London: Kluwer Academic Publishers; 2000. p. 221.
[3] Venkatesvaran H, Cakmak M. Polym Engng Sci 2001;41:341.
[4] Galay J, Cakmak M. J Polym Sci Part B: Polym Phys 2001;39(11): 1107–21.
[5] Galay J, Cakmak M. J Polym Sci Part B: Polym Phys 2001;39(11): 1147–59.
[6] Alberola N, Fugier M, Petit D, Fillon B. J Mater Sci 1995;30:860–8.
[7] Rettenberger S, Capt L, Munstedt H, Stopperka K, Sanze J. Rheol Acta 2002;41(4):332–6.
[8] Samuels RJ. J Polym Sci A-2 1967;6:1101–39.
[9] Flood JE, Nulf S. Polym Engng Sci 1990;30:1504–12.
[10] Okajima S, Homma K. J Appl Polym Sci 1968;12:411–23.
[11] Quirk RP, Alsamarraie MAA. In: Brandrup J, Immergut E, editors. Polymer handbook, 3rd ed. New York: Wiley; 1989. p. V/27–V/33.
[12] Beekmans F, Posthuma de Boer A. Macromolecules 1996;29: 8726–33.
[13] Gurnee EF. J Polym Sci A-2 1967;5:817–28.
[14] Masubuchi Y, Takimoto J, Koyama K. Seikei-Kakou 1999;11(2): 102–7.
[15] Alexander L. X-ray diffraction methods in polymer science. New York: Huntington; 1979. p. 247–9.
[16] Samuel J. Makromol Chem, Suppl 1981;4:241–70.
[17] Kobayashi Y, Okajima S, Narita A. J Appl Polym Sci 1967;11: 2515–23.
[18] Sen TZ, Toki S, Cakmak M. SPE ANTEC Tech Pap 2001;47(2): 1510–4.
[19] Samuels RJ. J Polym Sci C 1967;20:253–84.
[20] Samuels RJ. J Polym Sci A-2 1967;6:1101–39.
[21] Tashin JF. In: Ward IM, Coates PD, editors. Solid phase processing of polymers. Munich: Hanser; 2000. Chapter 6.
[22] Tadmor Z, Gogos CG. Principles of polymer processing. New York: Wiley; 1979. p. 52–4.
[23] Ishizuka O, Koyama K. Sen'I Gakkaishi 1976;32(2):T49–T54.